13

Intersubband Transitions in the Quantum Dot Layers for Quantum Confined Photodetector

Shiang-Feng Tang[1*], Tzu-Chiang Chen[2*],
Shih-Yen Lin[3*] and Hsing-Yuan Tu[4*],
[1]*Chung-Shan Institute of Science and Technology*
[2]*National Defense University*
[3]*Academia Sinica*
[4]*National Taiwan University*
Taiwan, R.O.C.

1. Introduction

In nanostructure like quantum dots (QDs) embedded in the spacing layer with high energy barrier, where electrons are three-dimensionally confined into nanometer-scale semiconductor structures, the novel physical characteristics are expected to emerge. The novel properties would greatly improve semiconductor device performance. Optoelectronic devices with quantum dot heterostructure like quantum dot infrared photodetector (QDIP) have already been proposed in the recent years. When QDs are incorporated into the layered structure of a semiconductor for optoelectronic device applications, electrical control is critical to the operation of device. It is desirable that both an electric field can be applied to change physical properties of the QDs embedded in the spacing layers i.e., the active region of the device and that the photo-induced carriers can be excited and transited to generate the photocurrent. In this chapter, The pseudopotential model of using multiple-quantum-dot (MQD) structures for detect infrared radiation can be explained by exploiting the basic principles of quantum mechanics, with the uniform and isotropic strain-induced potential to well simulate the electronic properties of InAs/In(Ga)As QDIP active region by finite element method (FEM). The vertically coupled and decoupled wave-functions of electrons on MQD with dependences of thickness of spacing layers are also calculated by means of the FEM. The method is ideally suited for numerical analysis by computer. The typical and particular QDIP structure are involved and introduced in this section. Here, the outstanding performance of the QDIP which has emerged as a potential alternative to QWIPs would be proposed. The motivation for interest in QDIPs is rooted in two characteristics of quantum dots. The first is that QDIPs are sensitive to normal-incident infrared radiation, a consequence of the 3-D confinement of electrons in the quantum dots. The other attribute is the weak thermionic coupling between the ground state and excited states. This should result in lower thermal excitation and, thus, lower dark current and higher operating temperature. The concomitant increase in the lifetimes of excited carriers should enable higher responsivities as carriers have more time to escape and contribute to the

photocurrent before relaxing to the ground state. Finally, the dependence of thickness of spacing layer affects enormously the coupling level of electron wave-function and the spectrum shifting of photon energy, where it is found to be consistent with experimentally measured intersubband transitions for the schemed QDIP.

2. Description of quantum-confined theory

An introduction into the electronic and optical properties of compound semiconductors in principle will be given. First a 3-dimensional (3D) volume is considered, followed by the lower dimensional structures and their quantum properties. The case of a quantum well (2D) will be first treated, because the principle of heterostructure properties can be explained with it. Quantum wire (1D) and quantum dot (0D) properties will then be derived in a similar way.

2.1 Wave-function in quantum structures (Alexander Weber, 1998)

2.1.1 3D bulk material

In a 3-dimensional crystal the movement of carriers (electrons, heavy holes or light holes) near to the band edge can be described as the motion of a quasi free particle, whose effective mass m* takes into account the interaction with the periodical lattice potential. In first approximation m* does not depend on the direction and a continuous energy spectrum of eigenvalues, which are isotropically distributed in the *k*-space, is obtained:

$$E^{3D}\left(\vec{k}\right)=\frac{\hbar^2}{2m^*}\left(k_x^2+k_y^2+k_z^2\right) \tag{1}$$

where k_x, k_y, k_z are the wavevectors along the *x*, *y* and *z*-axis.If the carriers are confined in lower dimensional systems such as 2-dimensional wells or 1-dimensional wires or 0D quantum dots with sizes of the order of the de Broglie wavelength of the carriers, a quantum structure in the electronic properties, for example the density of states, appears.

2.1.2 2D quantum well

For example in finite barrier, Fig. 1 shows the scheme of unstrained bandstructure of an InAs/$In_{0.52}Al_{0.48}As$ quantum well. Electrons and holes are trapped in the one-dimensional well, but can still move freely in the InAs layer. If the thickness of the active layer is of the order of the de Broglie wavelength of the carriers¸ Broglie = *hp* (*p* being the momentum of the carrier and *h* the Planck constant), quantum effects will appear, i.e., the quantization of the kinetic energy in the growth direction leads to discrete energy levels in the k_z direction in both the conduction band and the valence band.

The calculation of the eigenenergies in the confined structure using the effective mass approximation is now illustrated, with assuming that an idealized square, finite and symmetrical potential well with a thickness L_z and a potential energy

$$V_{well}\left(Z\right)=\begin{cases}0 & |z|<\dfrac{L_Z}{2}\\ -V_{well} & |z|>\dfrac{L_Z}{2}\end{cases} \tag{2}$$

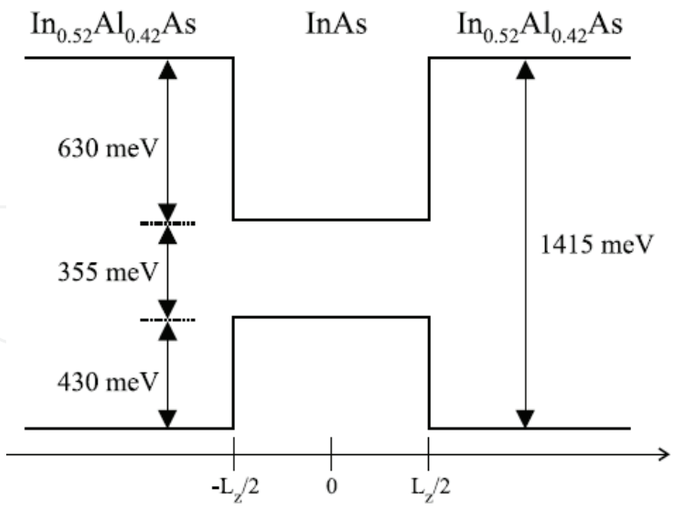

Fig. 1 Scheme of the band structure of InAs/$In_{0.52}Al_{0.48}As$.

The Schrödinger equation is:

$$\left[-\frac{\hbar^2}{2m}\Delta + v_{lattice(\vec{r})} + V_{well}(Z)\right]\Psi_{tot}(\vec{k},\vec{r}) = E(\vec{k})\Psi_{tot}(\vec{k},\vec{r}) \tag{3}$$

where V_{lattice} is the periodical, rapidly oscillating lattice potential, which describes the interaction of the carriers with the crystal lattice. Since it oscillates on a much smaller scale than the well potential V_{well}, it can be separated. This leads to the following wave-function:

$$\Psi_{tot}(\vec{k},\vec{r}) = \Psi_{env}(\vec{k},\vec{r}) \cdot \Phi_{B1}(\vec{k},\vec{r}) \tag{4}$$

The rapidly oscillating Bloch function Φ_{Bl} represents the carrier motion in the lattice potential, which can be handled with the introduction of an effective mass m^*. Ψ_{env} is the envelope function of the Bloch function and is determined by the slowly varying potential $V_{\text{well}}(z)$. Because $V_{\text{well}}(z)$ does not contain any terms in x or y, a second separation can be carried out:

$$\Psi_{env}(\vec{k},\vec{r}) = \Phi(\vec{k}_{x,y},\vec{r}_{x,y})\Theta(k_z,z) \tag{5}$$

where $\Phi(\vec{k}_{x,y},\vec{r}_{x,y})$ describes the motion in the 2 dimensions of the quantum well and leads to the energy eigenvalues:

$$E(\vec{k}_{xy}) = \frac{\hbar^2}{2m^*_{x,y}}(k_x^2,k_y^2) \tag{6}$$

with the effective mass $m^*_{x,y}$ for a motion in the layer plane.
In the z-direction a one dimensional Schrödinger equation for the motion of a free carrier with mass m^*_z in a symmetric quantum well $V_{\text{well}}(z)$ has to be solved:

$$\left[-\frac{\hbar^2}{2m_z^*}\frac{\partial^2}{\partial z^2}+V_{well}(Z)\right]\Theta(k_z,z)=E_z\Theta(k_z,z) \tag{7}$$

The following boundary conditions must be fulfilled:

1. $\Theta(k_z,z)$ is continuous everywhere;
2. by integrating equation (7) around any z_0, and for the specific potential of the square quantum well, $\frac{1}{m_z^*}\frac{d\Theta}{dz}$ is continuous everywhere;
3. $\lim_{z\to\pm\infty}|\Theta(k_z,z)|=0.$

The second condition accounts for the discontinuity of m^*_z at the boundary layers.
The solution of the Schrödinger equation is in this case:

$$\Theta(k_z,z)=\begin{cases}A\sin\left(\sqrt{\frac{2m_z^*E_{z,nz}}{\hbar^2}}-n_z\frac{\pi}{2}\right) & |z|\le\frac{L_z}{2} \qquad n_z=1,2,3.....\\ B\exp\left(-\sqrt{\frac{2m^*_{z,barrier}(v_{well}-E_{z,nz})}{\hbar^2}}\right) & |z|\ge\frac{L_z}{2}\end{cases} \tag{8}$$

with m^*_z and $m^*_{z,\text{barrier}}$ being the effective masses in z-direction inside the quantum well and inside the barrier, respectively.
In the barrier the wavefunction is exponentially attenuated while it oscillates in the quantum well. The ground state (nz= 1) is an even function and the higher states are alternately of even or odd parity.
The boundary conditions lead to a transcendental equation for the discrete energy levels $E_{z,nz}$ in k_z-direction, which can be solved numerically:

$$\tan\left(\sqrt{\frac{2m_z^*E_{z,nz}}{\hbar^2}}\frac{L_Z}{2}-n_z\frac{\pi}{2}\right)=-\sqrt{\frac{m^*_{z,barrier}E_{z,nz}}{m_z^*(v_{well}-E_{z,nz})}} \tag{9}$$

2.1.3 1D quantum wire

If the motion of the carriers is confined in further directions of space, the additional quantization can be calculated in a way analogous to that of the quantum well. For a one dimensional system (quantum wire) with infinite barriers the energy eigenvalues are:

$$E^{1D}_{n_x,n_z}(k_y)=\frac{\hbar^2\pi^2}{2}\left(\frac{n_x^2}{m_x^*L_Z^2}+\frac{n_Z^2}{m_Z^*L_Z^2}\right)+\frac{\hbar^2k_y^2}{2m_y^*} \tag{10}$$

The energy function is again a sum of discrete and continuous eigenvalues, which leads to an uni-dimensional subband structure.

2.1.4 0D quantum dot

For a parallelepipedic quantum dot one obtains:

$$E^{0D}_{n_x,n_z,n_z} = \frac{\hbar^2\pi^2}{2}\left(\frac{n_x^2}{m_x^* L_x^2} + \frac{n_y^2}{m_y^* L_y^2} + \frac{n_Z^2}{m_Z^* L_Z^2}\right) \tag{11}$$

where $(n_x, n_y, n_z) \in (\mathrm{N3})^*$ are the quantum numbers. They are integers, but not all of them are allowed to be 0. $L_{x,y,z}$ are the sizes of the structure and $m^*_{x,y,z}$ the effective masses in the respective directions.

The carriers in a quantum dot are completely localized and only discrete energy levels exist. In the realistic case of finite potential wells, numerical calculations must be performed to find an exact solution of the Schrödinger equation (Daniel Fritsch et al., 2003). In real situations, such as self organized quantum dots, exact calculations of the discrete energy levels proved to be very difficult and have only been performed numerically for the InAs /GaAs quantum dot system. First, the exact shape of the dot is usually not known (facets of pyramids, radii in lens shape, . . .). Second, anisotropic strain largely influences the electronic properties of 1D and 0D quantum structures.

Fig. 2 shows as an example the strain distribution for an InAs/GaAs quantum dot, which has the shape of a square pyramid. Far away form the dot in the wetting layer there is biaxial strain which is entirely confined in the wetting layer: because InAs has a smaller lattice constant than GaAs, in x and y direction the InAs layer is compressed (ε_{xx} and ε_{yy} are negative) and in the z direction a tension strain can be distinguished ($\varepsilon_{zz} > 0$). The strain distribution inside the pyramid is different. Close to the lower interface, ε_{zz} is still positive but much smaller than in the wetting layer because the substrate can no longer force the interface lattice constant to be that of the substrate. With increasing height within the dot, ε_{zz} changes its sign and becomes negative at the top of the pyramid. This happens because at the very top only small forces act on the quantum dot in the xy plane, but the GaAs barrier compresses the pyramid mainly from the sides along the z direction, imposing tensile strain components in the xy plane ($\varepsilon_{xx} = \varepsilon_{yy}$ become positive). Generally, however, the strain is still compressive even at the top of the pyramid ($T_{r\varepsilon} < 0$). Around the pyramid the barrier also becomes significantly strained (M. Grundmann et al., 1995). Because the strain distribution and the exact shape of the dots have to be known, calculating the correct electronic structure is difficult. Most approaches have been done using a $\vec{k}\cdot\vec{p}$ model (where $\vec{k}$ is the wave vector and $\vec{p}$ is the momentum) (S. L. Chuang & C. S. Chang, 1996). It calculates the $E(\vec{k})$ relationship over a small k range around the band extreme for multiple bands. Another approach considers the dot as a structure in its own right (rather than viewing it as a perturbation of the bulk material). The model is based on a pseudopotential framework (van de Walle and Chris G., 1989) and uses no adjustable parameters outside the bulk band structure. Fig. 3 shows the electron and hole wavefunction for the ground state and excited states for a self assembled InAs/GaAs system calculated with the pseudopotential framework. As expected the ground electron state wave function lays almost completely within the dot and covers a large part of it. However, excited states represent nodes with different shapes localized at the corners of the pyramid. Hence, the small dimensions of the dot and the presence of anisotropic strain have large effects on the form of the wavefunctions.

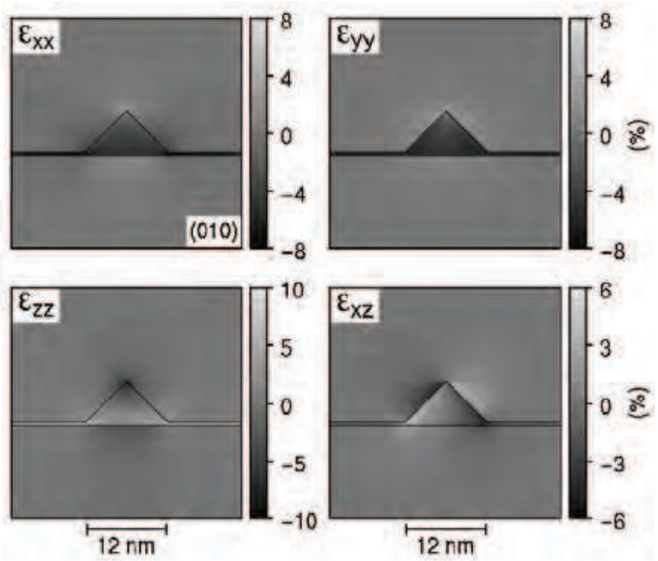

Fig. 2. Strain distribution in the (010) plane through the top of the pyramid of an InAs quantum dot grown on GaAs (O. Stier, M. et al., 1999)

Although the two approaches give a fair description of the hole and electron wavefunctions, the models strongly differ on the energetic structure of the dots especially for the excited states. They also do not account for the depletion of the wetting layer around the pyramids.

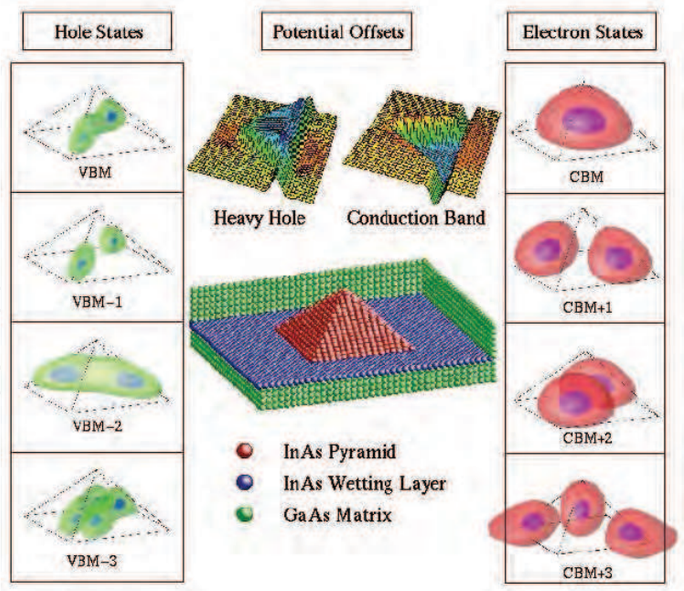

Fig. 3. The electronic structure of a strained InAs (110) pyramidal quantum dot embedded within GaAs. The strain-modified band offsets are shown above the atomic structure. They exhibit a well for both heavy holes and electrons. Isosurface plots of the four highest hole states and four lowest electron states, as obtained from pseudopotential calculations, appear

on the left and right. CBM means conduction band minimum and VBM valence band minimum.

2.2 Optical transitions

In this section, the main optical properties of low dimensional structures are discussed. The case of a single quantum well is firstly considered and lower dimensional structures are then treated in a similar way. Two kinds of optical transitions are considered (Fig. 4). Interband transitions take place between the conduction band and the valence band and involve two kinds of carriers (they are bipolar), electrons and holes. The energy of the transition is the bandgap energy plus the confinement energies of the electrons and holes minus the exciton binding energy. Intraband transitions happen inside either the conduction or the valence band and involve only one type of carrier (the transition is unipolar). In a quantum dot, intraband transitions occur between discrete energy levels. In quantum wells and quantum wires there exist subbands inside the conduction or the valence band. Intraband transitions in these structures between two subbands are called intersubband transitions. Note that another type of intraband transitions may occur which involves the transitions of a carrier from one subband to the same subband with absorption of a photon and emission of a phonon (momentum conservation). The latter is the analogue of free carrier absorption.

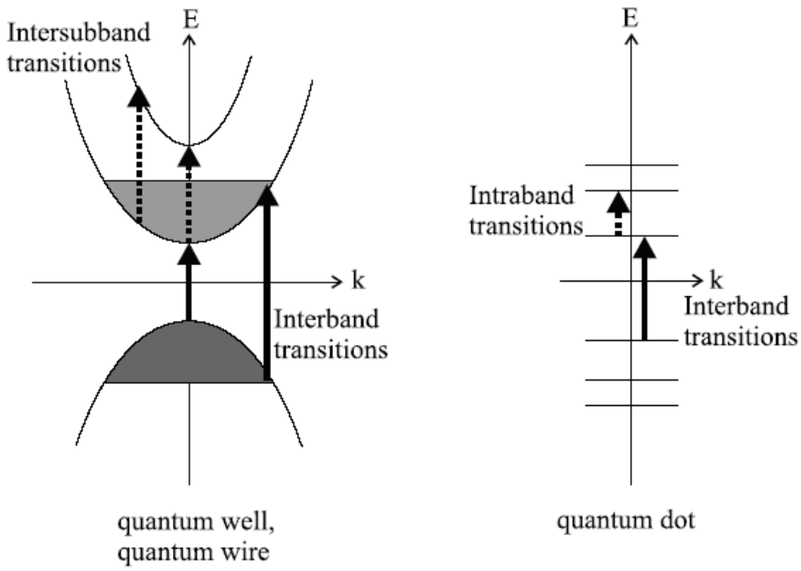

Fig. 4. Interband and intraband transitions for quantum wells, quantum wires (left) and quantum dots (right). The diagrams show a scheme of the band/level structure.

For 0D systems, there is *a priori* no forbidden direction but the actual polarization of intraband transitions between confined levels will depend on the spatial wave function symmetry of the states involved (see section 2.1.4), since the dipole is $\mu_{if} = e\left\langle \Psi_i \middle| \vec{\varepsilon} \cdot \vec{r} \middle| \Psi_f \right\rangle$. This means that the polarization of the intraband dipole can be predicted by means of

simple symmetry considerations. For example, the transition VBM→VBM-1 in Fig. 3 is polarized along the growth direction, whereas VBM→VBM-2 is polarized in the wetting layer plane. Normal incidence intraband absorption in quantum wells is usually forbidden. However, in quantum wires and quantum dots in-plane polarized transitions become possible, which is of great interest for the development of IR photodetectors irradiated at normal-incidence. Intraband spectroscopy is a validly experimental technique for investigating low dimensional semiconductors, since one can get insight on the confinement energies and on the spatial symmetries of the excited states, because the polarizations of the transitions can be measured (M. A. Cusack et al., 1997).

2.3 Oscillator strength

The oscillator strength of an intraband transition between the ground state and the first excited state is:

$$f = \frac{2m_0 E_{21}}{e^2\hbar^2}\mu_{12}^2 \tag{12}$$

where E_{21} is the energy difference between the two states. The oscillator strength of intersubband transitions does not depend on the energy of the transition, i.e., on the width of the quantum well, but only depends on the carrier effective mass which is material dependent: Because the intersubband energy $E_{21} \approx 3\hbar^2\pi^2/(2m^*L_z^2)$. Lower effective masses give larger oscillator strengths.

2.4 Intraband absorption

The intraband absorption coefficient for the 1→ 2 transition in a quantum structure can be expressed as (Shu-Shen Li, & Jian-Bai Xia, 1997):

$$\alpha(\omega) = \frac{\pi E_{21} e^2 (n_1 - n_2)}{2\varepsilon_0 c\tilde{n} m_0 \omega\Omega} \cdot f \cdot g(E_{21} - \hbar\omega) \tag{13}$$

where $n_1 \rightarrow n_2$ is the number of carriers, which can absorb in the active volume Ω of the quantum structure, ε_0 the dielectrical constant and $\check{n}$ the refractive index. f is the oscillator strength (equation (12)) and $g(\omega)$ is a lineshape function.

The spectral lineshape $g(\omega)$ takes into account several contributions:

- The homogeneous spectral width due to the finite coherence time between the two levels. This width can be expressed by a Lorentzian lineshape:

$$L(\omega) = \frac{1}{\pi}\frac{\hbar\Gamma}{(E_{21} - \hbar\omega)^2 + \hbar^2\Gamma^2} \tag{14}$$

  where $2\hbar\Gamma$ is the full width at half maximum (FWHM) of the intraband resonance.
- The inhomogeneous broadening caused by imperfections of the structure. In the case of a quantum well, imperfections are mainly variations of the width of the layer. For quantum wires and dots, size distributions of the structures are the origin of this lineshape broadening. For the example of quantum dots, this can be explained as followed: Smaller dots have higher energy levels and also greater differences between two states in one

'band', while greater dots possess smaller energy differences between two states. As the absorption takes place in a huge number of quantum dots, the sum of all their narrow absorption lines at different energy positions will be observed. The result is that the absorption spectrum overtakes the shape of the size distribution function of the dots.

- The inhomogeneous spectral width introduced by the non-parabolicity or, more general, by the coupling with other levels. This causes an asymmetric lineshape (K. Leifer et al., 2007).

3. Introduced finite element method for confined states and preparation of quantum confined structures for quantum dot infrared photodetector

3.1 Description of study background for strained InAs QDs embedded in surfactant $In_{0.1}Ga_{0.9}As$ within thickness-modified GaAs spacer layer

The analysis of strain effects in a quantum mechanical model of semiconductor devices has only recently been attempted by C. Pryor et al. (C. Pryor et al., 1998), Williamson et al., (A. J. Williamson et al., 2000) and Grundmann et al., who calculate strain-induced potentials and wave functions in quantum dots (QDs), and Gerhard Klimeck et.al (Gerhard Klimeck et al., 2002), who reviews the topic of electronic structure in dome-shaped semiconductor QDs based on atomistic methods. Few studies have made fitting with experimental measurements; Pistol et al. model strain effects on the band gap in buried QDs, which is consistent with photoluminescence (PL) data firstly. Models of semiconductor devices by means of the finite element method (FEM) have been proposed by a number of authors for one- and two dimensionally quantum-confined problems (G. R. Liu & S .S Quek Jerry, 2002, T. Benabbas et al., 1999),. The time–independent Schrödinger equation including the strain-induced potential is solved numerically by means of the finite element method to obtain the spectrum of energies and wave functions of available states. In the technique presented here, calculations of bandstructures on the heterostructure of QDs are well suited for the FEM, which is a common tool in continuum mechanics, to the best of our knowledge. The main idea of the method is that an unknown continuous field in the domain is represented approximately in terms of its values at discrete points (nodes) within the domain; the goal is to determine optimal values for these nodal quantities. The domain is covered with areas (in two dimensions) or volumes (in three dimensions) whose boundaries are defined geometrically by the nodes; these areas or volumes are the elements. Fields are defined within each element in terms of the values of the nodal quantities on its boundary by means of a suitable interpolation scheme. In the paper, the energy band levels and wave functions of InAs QDs buried in $In_{0.1}Ga_{0.9}As$/GaAs barriers have been calculated using a three-dimensional (3D) FEM formulation incorporated with the strained structures. In earlier publication (Tzu-Huan Huang et al., 2007), it is treated in the similar quantum structure with thicker GaAs spacer i.e., 30nm and the simplified without considering the vertically electronic coupling due to the larger barrier blockade and with the coherent QD geometry and constant spacing among the QDs. It is reasonable to infer that the multiple active QD regions are merely considered as increasing the intensity of photoluminescence (PL) and photoresponse (PR). By above assuming, earlier work is made with from single QD to the array of 9 QDs in a single layer for the calculation of electron and hole confined levels contrast to the established QDIP grown structure. The simulated results are agreed with the PL and PR experimental data. And the calculations of the interband and intraband

transitions can be well predicted the morphology of QD matrix to be consistent with the cross-sectional transmission electron microscopy (XTEM) images. The QD geometry is characterized to lens-shaped with 20 nm in base diameter and 3 nm in height.
Under our calculation, we have chosen to focus on the well-established 'lens-shaped' dot geometry, because the shape of QD is considered as the experimental TEM image, which is available in most cases of QD growth. In theoretical simulations based on the schematic 3-periodic QD structures as shown in Fig. 5, it is demonstrated that the 0, 1, 2, 3, 4 and 15 nm-thick undoped GaAs spacer/5 nm-thick undoped $In_{0.1}Ga_{0.9}As$ top surfactant/3 nm-nominal thick doped InAs QD/1 nm doped $In_{0.1}Ga_{0.9}As$ bottom surfactant as the active region and considered the influences on wave-functions of the vertically electronic inter-coupling mechanism due to the modified spacer layers.

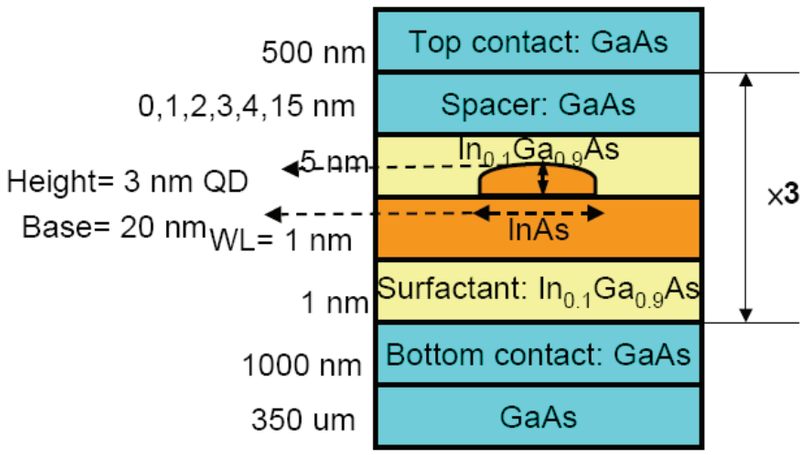

Fig. 5. The schematic 3 period of QD heterostructure with cross-sectional lens-shaped geometry.

In this section, we present a theoretical study of the electronic properties of these structures of self-assembled quantum dots (SAQD's) used the single-band effective mass approximation theory (EMA) to calculate the energy levels and wave-functions in $InAs/In_xGa_{1-x}As/GaAs$ lens-like shaped QDs. If the energy dispersion relation for a single band near k_0 ,i.e. the integration over k is mainly contributed from $k=k_0$ (an extremum or zone center), and is given by

$$E_n(k) = E_n(k_0) + \sum_{\alpha,\beta} \frac{\hbar^2}{2}\left(\frac{1}{m^*}\right)_{\alpha\beta} k_\alpha k_\beta \tag{15}$$

for the Hamiltonian H_0 with a periodic potential

$$H_0 = \frac{P^2}{2m_0} + V(r) \tag{16}$$

$$H_0\varphi_{nk}(r) = E_n(K)\varphi_{nk}(r) \tag{17}$$

then the solution for the Schrödinger equation with a perturbation $U(\mathbf{r})$ such as an impurity or well potential

$$\left[H_0 + U(r)\right]\varphi(r) = E\varphi(r) \tag{18}$$

is obtained by solving

$$\left[\sum_{\alpha,\beta}\frac{\hbar^2}{2}\left[\frac{1}{m^*}\right]_{\alpha\beta}(-i\frac{\partial}{\partial x_\alpha})(-i\frac{\partial}{\partial x_\beta}) + U(r)\right]F(r) = \left[E - E_n(K_0)\right]F(r) \tag{19}$$

for the envelope function $F(\mathbf{r})$ and the energy E. The wave function is

$$\varphi(r) = F(r)u_{nk_0}(r) \tag{20}$$

The most important result is that the periodic potential $V(\mathbf{r})$ determines the energy bands the effective masses, $\left(\frac{1}{m^*}\right)_{\alpha\beta}$, and the effective mass equation (Eq.19) contains only the extra perturbation potential $U(\mathbf{r})$, since the effective masses already take into account the periodic potential. The form of the Schrödinger equation to be solved on the finite element mesh is obtained by minimizing the total variation of the weak, or Galerkin form of the equation with respect to the wave function. The minimum in variation with respect to the wave function corresponds physically to a minimum energy. A general discussion of the variational formulation of the finite element method is given by H. T. Johnson et al., (H. T. Johnson et al. 1998). The functional corresponding to the weak form of the time-independent Schrödinger equation with a non-uniform potential is given by

$$\Pi(\Psi^{\alpha}) = \int_R \nabla\Psi^{\alpha} L^{\alpha\beta}\Psi^{\beta} dR + \int_R \Psi^{\alpha} V^{\alpha\beta}\Psi^{\beta} dR - E\int_R \Psi^{\alpha}\Psi^{\beta} dR \tag{21}$$

where Ψ^{α}, $L^{\alpha\beta}$, and $V^{\alpha\beta}$ are functions of position in the structure. The term $L^{\alpha\beta}$ is taken to be constant within each element of the mesh. The fields Ψ^{α}, $\Delta\Psi^{\alpha}$, and $V^{\alpha\beta}$ are represented by their nodal values. Values throughout each element are determined by interpolation according to the particular shape functions that are adopted. Fig.6 shows the mesh for this region with very highly refined in the neighboring QDs and wetting layer from single to the array of 9 QDs in one layer where large wave-function gradients are expected. The mesh size used in the calculations reported here results in a very accurate determination of the energies E and good spatial resolution of the wave-functions, particularly for the lower-energy states. Convergence of the method is found by comparing solutions for meshes with successively decreasing nodal separation. Element refinement is particularly important in the active region of the device, where the wave-function gradients are largest. Fig.7 shows unstrained and strained effects on band lineup and deformation potential on QD active

region, Considering without the strain effects, the confinement of electron or hole is determined by the corresponding band offset. It is worth to note that in the InAs region, the electron sees a potential well with depth 0.842 eV while the hole sees a potential well with depth 0.26 eV.

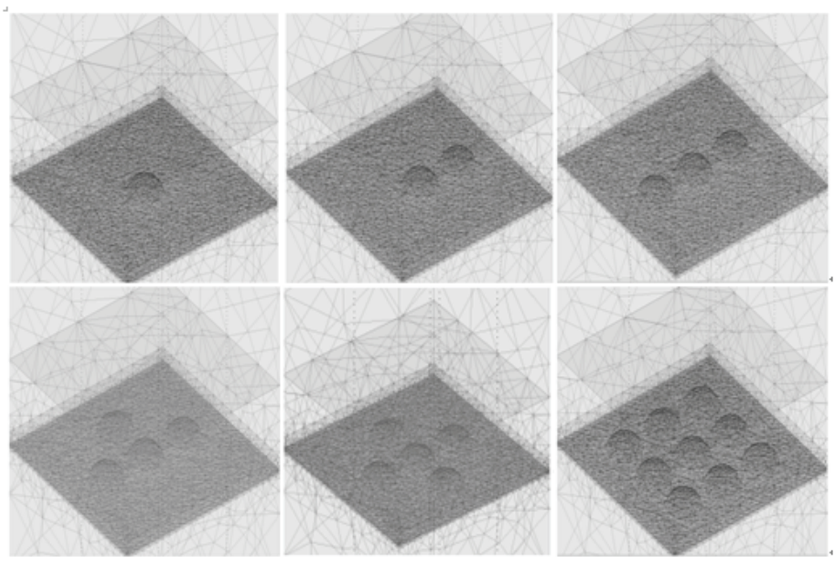

Fig. 6. The meshes in the neighboring quantum dots and wetting layer from single QD to the array of 9 QDs

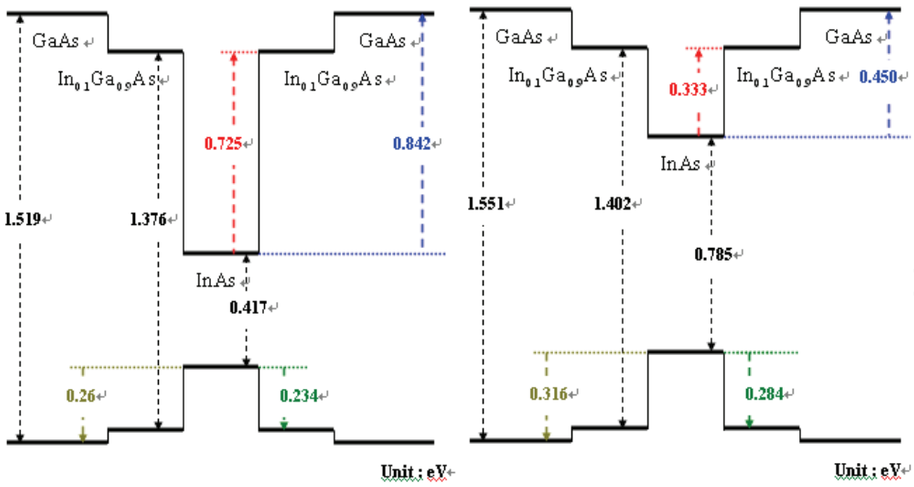

Fig. 7. Unstrained and strained effects on band lineup and deformation potential on QD active region

As well known, in the dot material, the compressive stress alters the curvature of the bulk bands causing the effective masses to differ from those of unstrained InAs. In our calculation we used the effective masses of bulk InAs under the average hydrostatic strain

present in the dot material. These values were obtained by performing semi-empirical pseudo-potential bandstructure calculations for the conduction-band valence band momentum matrix elements of InAs under strained effect. In the conduction band, these calculations yield a value for the effective mass of 0.04 m_0, a factor of two larger than in unstrained InAs of 0.023 m_0. The same trend is recovered in *ab initio* local-density calculations. However, the ab initio mass in InAs is too high and the empirical pseudo-potential result is more representative. In the absence of strain effects, the confining potential for an electron (hole) is a square well formed by the difference in the absolute energy of the conduction (valence)–band edges in InAs and GaAs. In each conventional cubic unit cell, the confining potential for each carrier type is shifted due to the strain. Since the strain varies from cell to cell, the confining potentials will also vary from cell to cell. Furthermore, degeneracies in the valence-band edge will be lifted due to deviations of the unit cells from axis symmetry. For each unit cell, the strain-induced shifts to the confining potentials are obtained by diagonalizing the 8×8 strain Hamiltonian matrix. Hence, the confining potentials including the effects of strain are piecewise continuous functions of position generated by our calculation. The compressive strain in the barrier shifts the GaAs conduction-band edge (at 1.551 eV) slightly above the unstrained level (at 1.519 eV) as shown in Fig.7.

It is assumed that the strain was taken to be a constant value between the InAs quantum dots and the surrounding InGaAs capping layer, oppositely, invalid in the surrounding GaAs spacer layer. And the main parameters including electron and heavy hole in the conduction and valence band of QD active region are listed in Table 1 and Table 2. The electron effective masses of each material system are summarized in Table1, M_GaAs, M_InGaAs_E and M_InAs_E are the electron effective masses in GaAs , InGaAs, and InAs materials, respectively. The heavy hole effective masses of each material system are summarized in Table2, M_GaAs_H, M_InGaAs_H and M_InAs_H are the heavy hole effective masses in GaAs , InGaAs, and InAs materials, respectively. The barrier height between GaAs and $In_{0.1}Ga_{0.9}As$ for electron is V1_E, oppositely, between InAs and $In_{0.1}Ga_{0.9}As$ is V2_E, and the value is 0.450 eV and 0.333 eV, respectively.

Paremeters	Values	Unit	Descriptions
C1	3.81	eV/Å	Differential coefficient $\hbar^2/2m_0$
M_GaAs_E	0.0665	m_0	Effective electron mass in GaAs, m_0 is free electron mass
M_InGaAs_E	0.064	m_0	Effective electron mass in $In_{0.1}Ga_{0.9}As$
M_InAs_E	0.04	m_0	Effective electron mass in InAs
V1_E	0.450	eV	Conduction band-edge difference between GaAs and InAs
V2_E	0.333	eV	Conduction band-edge difference between $In_{0.1}Ga_{0.9}As$ and InAs

Table 1. Simulated parameters for electron in conduction band edges (Being taken the strained effect into account)

Paremeters	Values	Unit	Descriptions
C1	3.81	eV/Å	Differential coefficient $\hbar^2/2m_0$
M_GaAs_H	0.3774	m_0	Effective hole mass in GaAs, m_0 is free electron mass
M_InGaAs_H	0.374	m_0	Effective hole mass in $In_{0.1}Ga_{0.9}As$
M_InAs_H	0.341	m_0	Effective hole mass in InAs
V1_H	0.316	eV	Valence band-edge difference between GaAs and InAs
V2_H	0.284	eV	Valence band-edge difference between $In_{0.1}Ga_{0.9}As$ and InAs

Table 2. Simulated parameters for heavy hole in valence band edges (Being taken the strained effect into account)

In the process of simulation, the conduction band-energy difference between $In_{0.1}Ga_{0.9}As$ and InAs is considered as 0.333 eV, similarly, 0.284 eV in valence band-energy difference. In the confined energy, the bound-states would be considered and extracted, once, excess the confined barrier, it is taken as non-bounded states outer QD.

3.2 Preparation for strained quantum dot infrared photodetector

The QDIP structure based on $In_{0.1}Ga_{0.9}As/GaAs$ material system was grown on a (001) semi-insulting GaAs substrate by using the Riber Epineat solid-state molecular beam epitaxy (MBE) system. The samples of 30 periodic 3 ML InAs QD matrax on 1nm $In_{0.1}Ga_{0.9}As$ surfactant layer sandwiched between 5 nm $In_{0.1}Ga_{0.9}As$ and 30 nm GaAs structures with InAs QD region Si-doped to 1×10^{18} cm^{-3}. The detailed device structure and fabricated processing have been mentioned and similar to those previously proposed. Specially, it is to be noted that using the lower growth temperature of ~480 ℃ for nucleating InAs dots on GaAs substrate and As flux ≒ 80 mil (equivalent V/III ratio≦2) incorporated with 10 sec of growth interruption, the two dominant groups of InAs quantum dot matrix has been achieved and shown in Fig. 8.

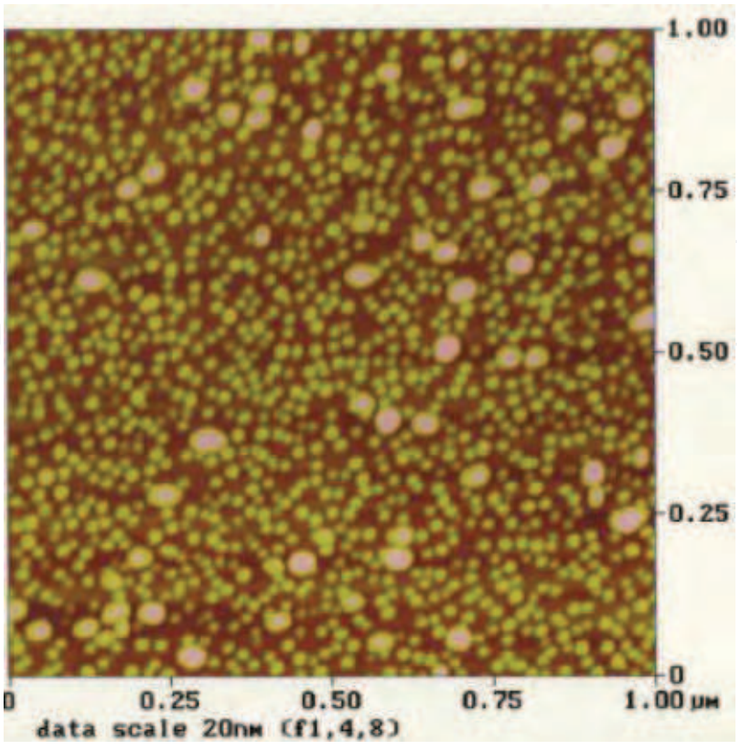

Fig. 8. The 2-diminsional 1μm×1μm AFM image with bimodal QD populations.

The 2-D morphology image is taken by DI-2000 atomic force microscopy (AFM) series. The larger and smaller-sized dot densities are 1.5×10^{10} and 2.5×10^{11} cm^{-2}, respectively. The QD lateral size and height of the two populations are 20 and 5 nm for smaller ones, 50 and 15 nm for larger ones. Due to introducing the mediate layer of 1 nm-thick $In_{0.1}Ga_{0.9}As$ under the growth temperature higher ~20℃ than that of QD and grown below the InAs QD nucleation, the surfactant layer results in high size-uniformity of QD bimodality and better epitaxial performance. Bias-dependent spectral response for the testing device measured using a Perkin-Elmer spectrum one fast Fourier-transform IR (FTIR) spectroscopy coupled with a cryostat under the normal incident scheme. The photoresponse signals were corrected by an absolute blackbody radiation source shown in Fig 9

Fig. 9. The physical FTIR and cryostat systems for temperature-dependent photoresponse measurement

4. Results of the quantum mechanical calculation with finite element method and the discussion as comparison with the experimental data

4.1 Iso-surface probability distribution for electron density of state within 3 periods of QD matrix layers calculated by finite element method

While 9 QDs are situated within 100 nmx100 nm of $In_{0.1}Ga_{0.9}As/GaAs$ unit-cell area, the equivalent dot density in each QD matrix is $9x10^{10}cm^{-2}$, as shown in Fig.6, which is comparable with that extracted from the experimental AFM image previously.

For three-dimensional FEM quantum mechanical calculations, the synthetic influences of strained interfaces of $GaAs/In_{0.1}Ga_{0.9}As/InAs$ in this work have been considered as the deformation potentials of the band offset (*i.e.*, called as band differences) to simplify the complexity of heterostructure modeling treated by the dual-cored pentium CPU. A theoretical model is first presented by Chris G. Van de Walle (Van de Walle and Chris G., 1989) to predict the band offset at pseudomorphic strained layer interfaces. The theory is based on the local-density-functional pseudopotential formalism and the model-solid approach of C. G. Van de Walle and R. M. Martin (Chris G. Van de Walle & R. M. Martin, 1986). The model can be most simply expressed in terms of an absolute energy level for each accounted for semiconductor system and deformation potentials that describe the effects of strain on the electronic bands. The model has been explored well that combinations of semiconductor materials and configurations of strains will lead to the desired electronic properties. Accordingly, using the previously mentioned and simply pseudopotential model attributed to the strained heterostructures, the differences of energy band-edges in InAs/InGaAs/GaAs material system are deformed from 0.842 ($\Delta E_{c\ GaAs\text{-}InAs}$) and 0.725 eV ($\Delta E_{c\ In0.1Ga0.9As\text{-}InAs}$) to shrink into 0.45 and 0.333 eV, respectively as seen in Fig. 7 and Table 1. However, it interesting to note that valence band offsets are enlarged in contrast with the differences of conduction band-edges. It may be explained that enlarging valence band

offsets attribute to the heavy and light hole mixing due to the strain inducement. These modified parameters for valence bands are shown in Fig. 7 and Table 2. The isotropic strains are assumed to simplify the calculation of confined states within active regions while using finite element approximation (FEA). Based on these parameters being taken account for isotropic strain effect on the interfaces between the lattice-mismatch materials, and modifying thickness from 0, 1, 2, 3, 4 to 15 nm of GaAs spacing layers, and under given 0.45 eV of the overall confined energy barrier in active region for conduction band, the eigenvalues versus quantum-confined numbers are calculated as shown in Fig. 10 and the deviation of spacing layer within 0 ~15 nm is indistinctive for extracting the eigenvalues

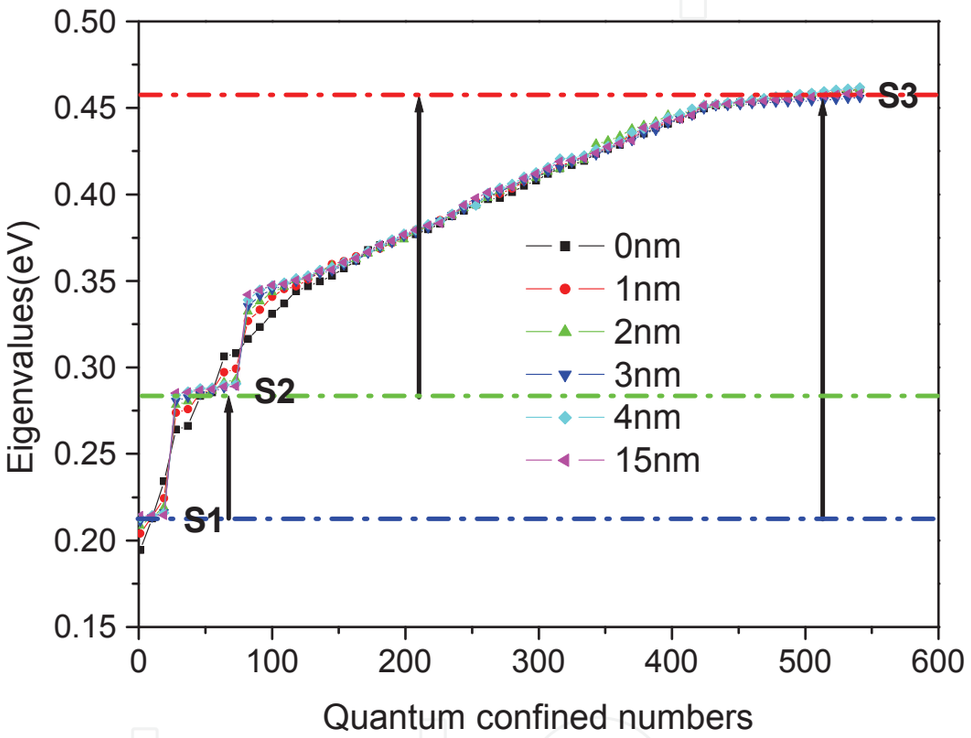

Fig. 10. The eigenvalues versus quantum-confined numbers with thickness from 0, 1, 2, 3, 4 to 15 nm of GaAs spacing layers under given 0.45 eV of the overall confined energy barrier in active region for conduction band

The electrical field of a light wave with frequency ω and wavevector $\vec{k}$ $(|k|) = \frac{n\omega}{c}$ can be expressed as

$$\vec{F}(\vec{r},t) = F\vec{\varepsilon}\cos(\omega t - \vec{k}\cdot\vec{r}) \tag{22}$$

with $\vec{\varepsilon}$ being a supposed linear polarization. In the Coulomb gauge (div $\vec{A}$ = 0), the

electrical field depends on the vector potential $\vec{A}$ as follows:

$$\vec{F} = -\frac{1}{c}\frac{\partial \vec{A}}{\partial t} \tag{23}$$

This leads to

$$\vec{A}(\vec{r},t) = -\frac{\vec{\varepsilon}\, cF}{2i\omega}\left[\exp(i(\omega t - \vec{k}\cdot\vec{r})) - \exp(-i(\omega t - \vec{k}\cdot\vec{r}))\right] \tag{24}$$

The one electron Hamiltonian of a heterostructure in presence of an electromagnetic field is in first approximation:

$$H = H_0 + \frac{e}{2m_0 c}(\vec{p}\cdot\vec{A} + \vec{A}\cdot\vec{p}) \tag{25}$$

with the electron momentum $\vec{p}$ and the electron charge *e*.
The probability of an optical stimulated transition is given by Fermi's golden rule:

$$\widetilde{P}_{if} = \frac{2\pi}{\hbar}\left|\langle f|V|i\rangle\right|^2 \cdot \delta(\varepsilon_f - \varepsilon_i - \hbar\omega) \tag{26}$$

where V is the perturbation term of the Hamiltonian $H = H_0 + V$. Under the electric dipole approximation, $\left(\exp\left(-i\vec{k}\cdot\vec{r}\right)\right) \approx 1$ which is valid for visible and infrared wavelengths, V is:

$$V = \frac{ieF}{2m_0\omega}\vec{\varepsilon}\cdot\vec{p} \tag{27}$$

If the quantum states *i* and *f* are partially occupied, the transition probability has to be weighted by the occupancy factor given by the Fermi distribution $f(\varepsilon)$:

$$P_{if} = \widetilde{P}_{if} f(\varepsilon_i)\left[1 - f(\varepsilon_f)\right] \tag{28}$$

where the Fermi distribution is the mean occupancy of the state ν:

$$f(\varepsilon_\nu) = \left[1 + \exp\left(\frac{1}{\kappa_B T}(\varepsilon_\nu - \mu)\right)\right]^{-1} \tag{29}$$

When taking into account the transitions $i \to f$ and $f \to i$, the linear absorption coefficient is

given by:

$$\alpha(\omega) = A\sum_{i,f}\frac{1}{m_0^*}\left|\vec{\varepsilon}\cdot\vec{p}_{if}\right|^2\partial\left(\varepsilon_f-\varepsilon_i-\hbar\omega\right)\left[f\left(\varepsilon_i\right)-f\left(\varepsilon_f\right)\right] \tag{30}$$

with $\vec{p}_{if}=\left\langle i\left|\vec{p}\right|f\right\rangle$, which contains the selection rules information, and $A=\frac{4\pi^2e^2}{ncm_0\omega\Omega}\cdot\Omega=SL$ is the irradiated volume of the sample.

The eigenvalues in the quantum-confined structures are derived by 3-D FEM formulations and equations (22) to (30), followed by Fermi-golden rule. It is obviously to note that more than one quantum-confined numbers in S_1, S_2 and S_3 regions associated with given similar eigenvalues, respectively. This phenomenon is known as degeneracy. The density of states of previously mentioned S regions are denser than the others. It means that higher transition probability has to be weighted by the occupancy factor given by the Fermi distribution $f(\varepsilon)$ which is followed by equations from (28) to (30). So, based on the theory of optical transition of quantum-confined structure, the transitions of $S_1\rightarrow S_2$, $S_2\rightarrow S_3$, and $S_1\rightarrow S_3$ are the most possibility for intraband transitions. The peak-wavelength positions from these 3 selection routes of optical transitions with 0 to 15 nm-thick GaAs spacing layers can be calculated and are listed in Table 3. Furthermore, according to Eq. (12), (13), and (14) associated with simplified calculations partly which are quoted from absorption spectrum of quantum well model, the absorption efficiencies versus wavelength from $S_1\rightarrow S_2$, $S_2\rightarrow S_3$, $S_1\rightarrow S_3$, and summation of above 3 routes are shown in Fig. 11. The results of absorption spectrum are well agreed with the data simulated by 3-dimensional quantum-confined FEM shown in Fig. 10 and Table 3.

Intraband Transitions \ Spacing thickness (nm)		0	1	2	3	4	15
S1-S3	E_{s1}-E_{s3} (eV)	0.2421505	0.242467	0.242726	0.239903	0.242553	0.240944
	λ_T (μm)	5.1207815	5.114108	5.108633	5.168763	5.112292	5.146414
S2-S3	E_{s2}-E_{s3} (eV)	0.1702775	0.170167	0.170794	0.168091	0.169357	0.168045
	λ_T (μm)	7.2822288	7.286958	7.2602	7.376972	7.321804	7.37897
S1-S2	E_{s1}-E_{s2} (eV)	0.071873	0.0723	0.071932	0.071812	0.073196	0.072899
	λ_T (μm)	17.252654	17.15088	17.23846	17.26731	16.94093	17.00976

Table 3. The peak-wavelength positions from these 3 selection routes of possible optical transitions with 0, 1, 2, 3, 4 and 15 nm-thick GaAs spacing layers

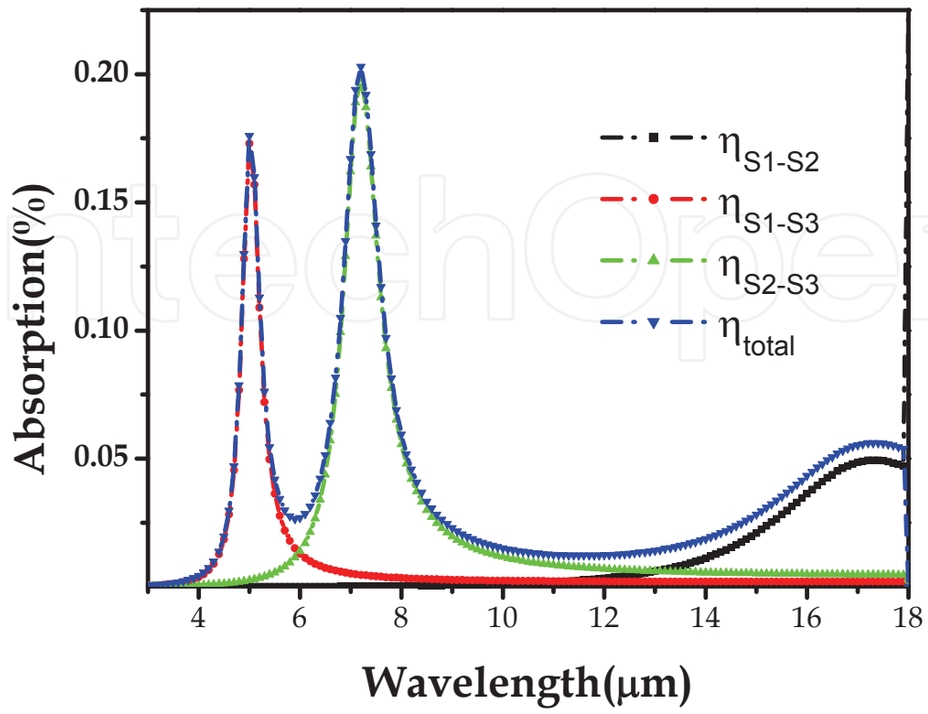

Fig. 11. Calculated absorption efficiencies versus wavelength for 3 periodic InAs QD matrix embedded in $In_{0.1}Ga_{0.9}As$/GaAs layers

The isosurface wave-functional distributions of electrons confined from ground to top-lying excited states for free GaAs spacing layer *i.e.,* electrons confined between InAs and GaAs conduction band edge minimum are shown as Fig. 12 (a) in 3-D and (b) in 2-D y-z in-plane view, respectively. Similarly, the isosurface wave-functional distributions of electrons confined from ground to top-lying excited states for 3 and 15 nm GaAs spacing layer *i.e.,* electrons confined between InAs and GaAs conduction band edge minimum are shown as Fig. 13 and 14 (a) in 3-D and (b) in 2-D y-z in-plane view, respectively. It is very interesting to observe that the wave-functions are lateral coupling easily in more top-lying excited states due to barrier lowering for higher confined states. While the thickness of GaAs spacing layer is larger than 3 nm, there are no vertical wave-couplings within the interlayers attributed to the barrier blockade of thicker GaAs spacing layer.

The similar structure based on Fig. 5 except for more than numbers of active layer are used to perform a standard semiconductor process as QDIP for spectrum measurement as mentioned section 3.2. Normal-incident photoresponsivity versus wavelength in 80K are measured and achieved from Eq. (13), (14), (28) to (30) and used the physical model from H. C. Liu are included (H. C. Liu, 1993), the simulated results can successfully interpret the measured photoresponse spectrum as shown in Fig. 15. The broadening dual-band peak wavelengths of 5.32 and 7.38 μm for the QDIP mainly originate from the interlevel transitions due to contributions of the degeneracy of engenlevels confined in the quantum heterostructure. The other partly attributes to QD sized distributions.

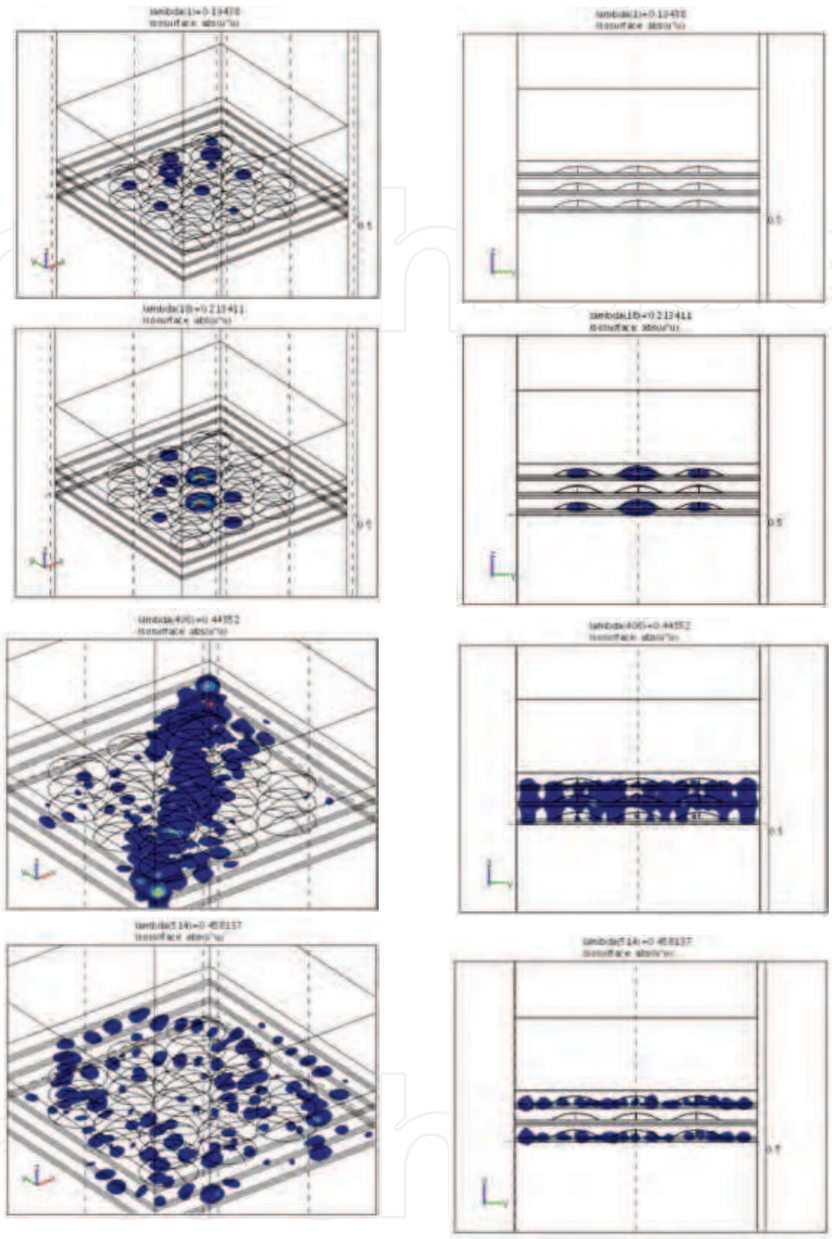

Fig. 12. Isosurface wave-functional distributions of electrons confined from ground to top-lying excited states for free GaAs spacing layer *i.e.,* electrons confined between InAs and GaAs conduction band edge minimum (a) in 3-D and (b) in 2-D y-z in-plane view

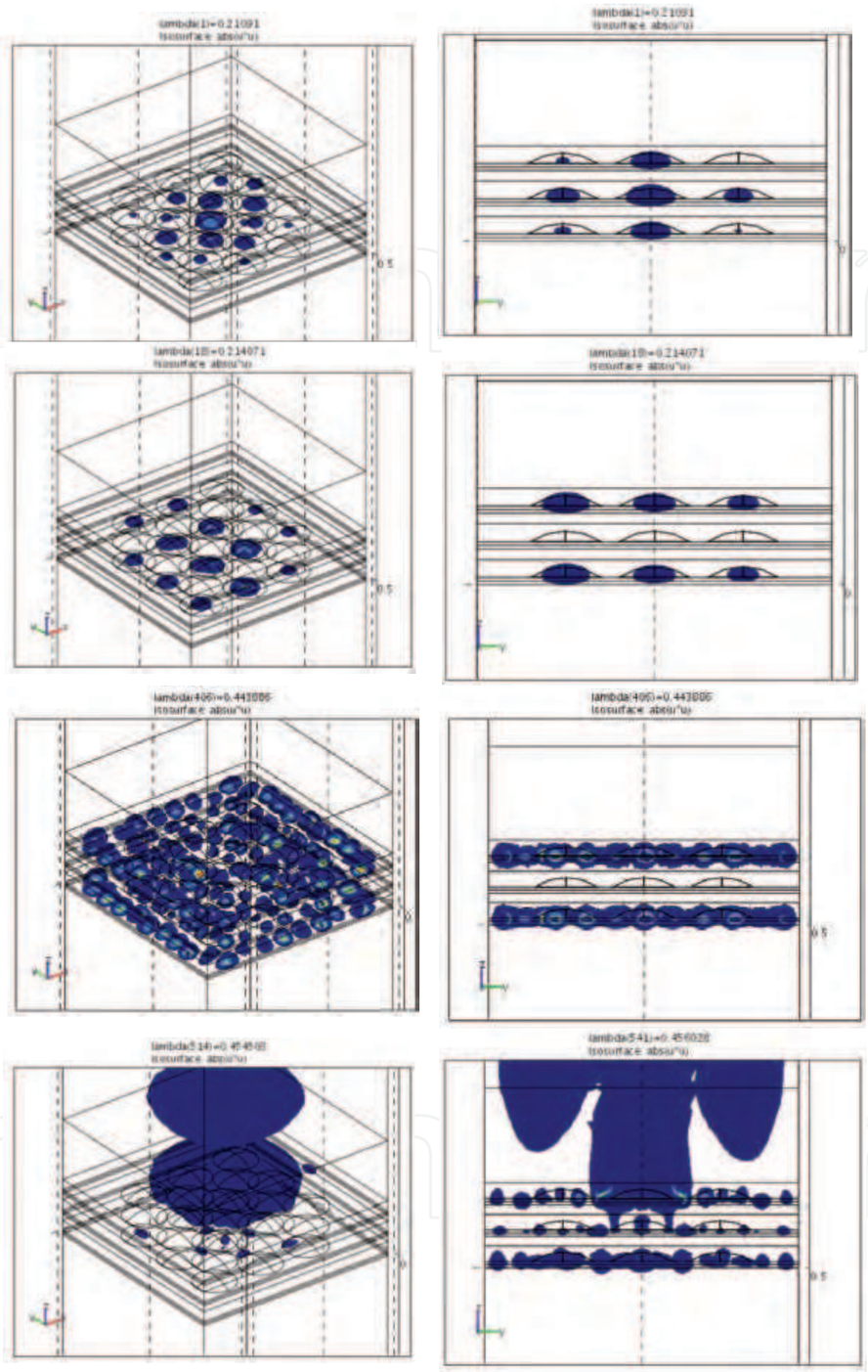

Fig. 13. Isosurface wave-functional distributions of electrons confined from ground to top-lying excited states for 3 nm-thick GaAs spacing layer *i.e.,* electrons confined between InAs and GaAs conduction band edge minimum (a) in 3-D and (b) in 2-D y-z in-plane view

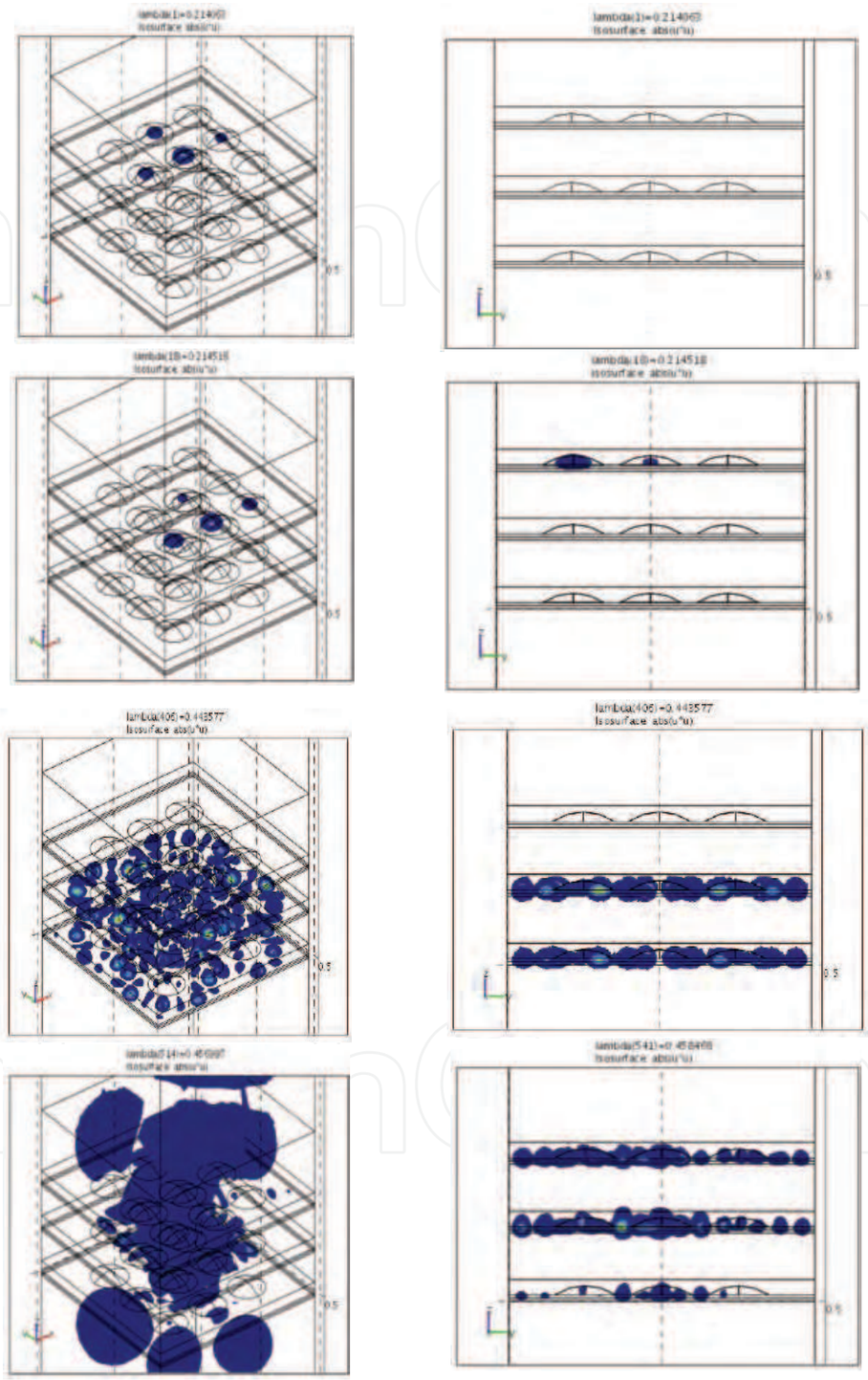

Fig. 14. Isosurface wave-functional distributions of electrons confined from ground to top-lying excited states for 15 nm-thick GaAs spacing layer *i.e.,* electrons confined between InAs and GaAs conduction band edge minimum (a) in 3-D and (b) in 2-D y-z in-plane view

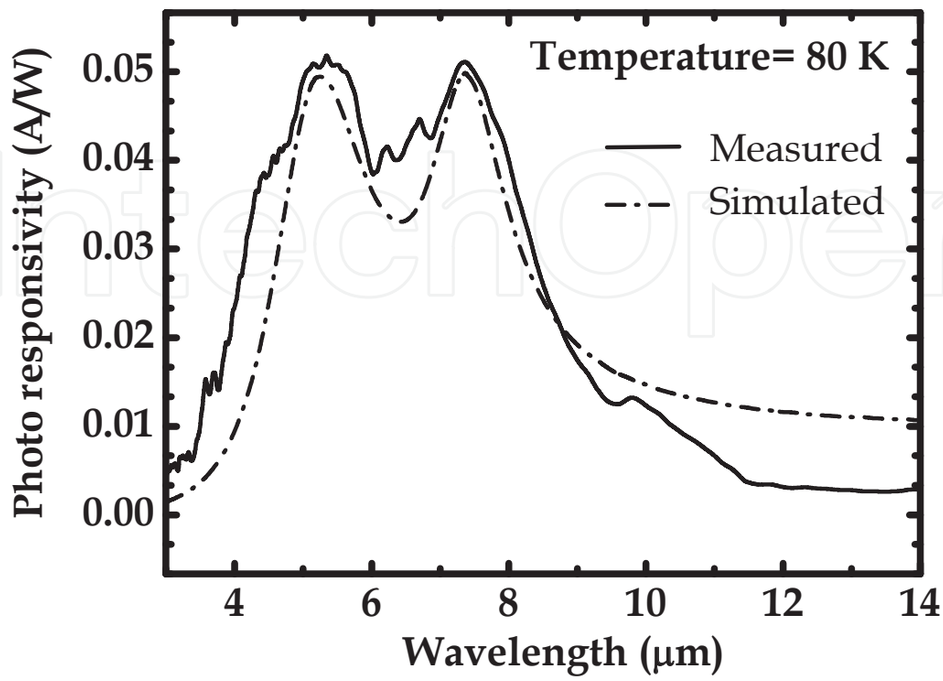

Fig. 15. The simulated results and measured photoresponse spectra

5. Conclusions

Intraband absorption coefficient with InAs/$In_{0.1}Ga_{0.9}As$ QDs covered with GaAs quantum is wells studied. The numerical values of photoinduced-intraband absorption spectra in multiple QDs layers are derived to achieve the three degeneracy regions by 3-dimensional quantum-confined FEM, which are well consistent with analytic absorption coefficient calculated from total intraband absorption coefficient $\alpha_{total}(\omega) = \sum_{i,f} \frac{\pi E_{fi} e^2 (n_i - n_f)}{2\varepsilon_0 c\tilde{n} m_0 \omega \Omega} \cdot f \cdot g(E_{fi} - \hbar\omega)$ which is inferred from the dipole $\mu_{if} = e\left\langle \Psi_i \middle| \vec{\varepsilon} \cdot \vec{r} \middle| \Psi_f \right\rangle$, and optical oscillator strength $f = \frac{2m_0 E_{21}}{e^2 \hbar^2} \mu_{12}^2$. Experimental results on photoresponse spectra combined with inter-leveling electron transitions agree satisfactorily with theory for the first time.

6. References

A. J. Williamson, L. W. Wang, and Alex Zunger (2000) "Theoretical interpretation of the experimental electronic structure of lens-shaped self-assembled InAs/GaAs quantum dots" *Physical Review B*, Vol. 62, No. 19, March 2000, pp.12963-12977

Alexander Weber (1998). "Intraband spectroscopy of semiconductor quantum dots", *Dissertation, Dr. of Phylosophy,* Julius-Maximilians-Universität, Wűrzburg

Chris G. Van de Walle and Richard M. Martin (1989) "Theoretical calculations of semiconductor heterojunction discontinuities"*J. Vac. Sci. Technol. B* .Vol. 4, No. 4, July 1986, pp. 1055-1059

C. Pryor, J. Kim, L. W. Wang, A. J. Williamson, and A. Zunger (1998) "Comparison of two methods for describing the strain profiles in quantum dots"*Journal of Applied Physics,* Vol. 83, March 1998, pp.2548-2550

Daniel Fritsch, Heidemarie Schmidt, and Marius Grundmann (2003)."Band-structure pseudopotential calculation of zinc-blende and wurtzite AlN, GaN, and InN", *Physical Review B*, Vol. 67, No. 4, June 2003, pp. 235205-1-13

Gerhard Klimeck, Marek Korkusinski, Haiying Xul, Seungwon Lee, Sebastien Goasguen, and Faisal Saied (2002). "Atomistic simulations of long-range strain and spatial asymmetry effects in multimillion-atom single and double quantum dot nanostructures", *Computer Modeling in Engineering and Science* , No. 3, February 2002, pp. 601

G R Liu and S S Quek Jerry (2002). "A finite element study of the stress and strain fields of InAs quantum dots embedded in GaAs", *Semiconductor Science and Technology,* Vol. 17, May 2002, pp. 630-643

H. C. Liu (1992). "Dependence of absorption spectrum and responsivity on the upper state position in quantum well intersubband photodetectors" *Journal of Applied Physics*, Vol. 73, No. 6, March 1992, pp. 3062-3067

H. T. Johnson, L. B. Freund, C. D. Akyüz, and A. Zaslavsky (1998). "Finite element analysis of strain effects on electronic and transport properties in quantum dots and wires", *Journal of Applied Physics*, Vol. 84, No. 7, October 1998, pp. 3714-3725

K. Leifer, E. Pelucchi, S. Watanabe, F. Michelini, B. Dwir, and E. Kapon (2007). "Narrow (≈ 4 meV) inhomogeneous broadening and its correlation with confinement potential of pyramidal quantum dot arrays", *Applied Physics Letters*, Vol. 91, No. 8, August 2007, pp. 81106-81108

M. A. Cusack, P. R. Briddon, and M. Jaros (1997). "Absorption spectra and optical transitions in InAs/GaAs self-assembled quantum dots", *Physical Review B*, Vol. 56, No. 7, August 1997, pp. 4047-4050

M. Grundmann, O. Stier, and D. Bimberg (1995)."InAs/GaAs pyramidal quantum dot: strain distribution, optical phonon, and electronic structure ", *Physical Review B*, Vol. 52, No. 16, October 1995, pp. 11969-11981

O. Stier, M. Grundmann, and D. Bimberg (1999)."Electronic and optical properties of strained quantum dots modeled by 8-band k·p theory", *Physical Review B*, Vol. 59, No. 8, February 1999, pp. 2688-2701

Shu-Shen Li and Jian-Bai Xia (1997) "Intraband optical absorption in semiconductor coupled quantum dots" *Physical Review B*, Vol. 55, No. 23, January 1997, pp.15434-15437

S. L. Chuang and C. S. Chang (1996) "k·p method for strained wurtzite semiconductors", *Physical Review B*, Vol. 54, No. 4, July 1996, pp. 2491-2504

Tzu-Huan Huang, Shiang-Feng Tang, Tzu-Chiang Chen, Fu-Fa Lu and Cheng-Der Chiang (2007) "Calculations of bandstructures on the lens and pyramid-shaped InAs quantum dot for confirming the photoluminescence and photoresponse" *Proceedings of SPIE,* Vol. 6479, February 2007, San Jose, CA, USA

T. Benabbas Y. Androussi, and A. Lefebvre (1999) "A finite-element study of strain fields in vertically aligned InAs islands in GaAs" *Journal of Applied Physics,* Vol. 86, May 1999, pp.1945-1948

van de Walle and Chris G. (1989) "Band lineups and deformation potentials in the model-solid theory" *Physical Review B*, Vol. 39, No. 3, January 1989, pp. 1871-1883

Cutting Edge Nanotechnology

Edited by Dragica Vasileska

ISBN 978-953-7619-93-0
Hard cover, 444 pages
Publisher InTech
Published online 01, March, 2010
Published in print edition March, 2010

The main purpose of this book is to describe important issues in various types of devices ranging from conventional transistors (opening chapters of the book) to molecular electronic devices whose fabrication and operation is discussed in the last few chapters of the book. As such, this book can serve as a guide for identifications of important areas of research in micro, nano and molecular electronics. We deeply acknowledge valuable contributions that each of the authors made in writing these excellent chapters.

How to reference

In order to correctly reference this scholarly work, feel free to copy and paste the following:

Shiang-Feng Tang, Tzu-Chiang Chen, Shih-Yen Lin and Hsing-Yuan Tu (2010). Intersubband Transitions in the Quantum Dot Layers for Quantum Confined Photodetector, Cutting Edge Nanotechnology, Dragica Vasileska (Ed.), ISBN: 978-953-7619-93-0, InTech, Available from: http://www.intechopen.com/books/cutting-edge-nanotechnology/intersubband-transitions-in-the-quantum-dot-layers-for-quantum-confined-photodetector

INTECH
open science | open minds

InTech Europe
University Campus STeP Ri
Slavka Krautzeka 83/A
51000 Rijeka, Croatia
Phone: +385 (51) 770 447
Fax: +385 (51) 686 166
www.intechopen.com

InTech China
Unit 405, Office Block, Hotel Equatorial Shanghai
No.65, Yan An Road (West), Shanghai, 200040, China
中国上海市延安西路65号上海国际贵都大饭店办公楼405单元
Phone: +86-21-62489820
Fax: +86-21-62489821

IntechOpen